In-situ Raman investigations of Fe-coated Ni OER electrodes

Ilias Efthimiopoulos[1*†], Sihan Zhang[1,2†], Nafiseh Samisereht[1], S. A. Sharat[1], Petra Ebbinghaus[1], Caroline Mehrmann[1], and Martin Rabe[1*]

[1]Max Planck Institute for Sustainable Materials, Max-Planck-Str. 1, 40237 Düsseldorf, Germany

[2]College of Chemistry, Nankai University, Tianjin 300071, China

Abstract

We have investigated the OER performance of Fe-coated Ni meshes via direct immersion of the samples in selected Fe-bearing solutions. In all cases, we were able to detect an enhancement of the OER performance, with the NM samples immersed in 20 mM $Fe(NO_3)_3$ and 20 mM $FeCl_2$ solutions showing the best activity. The stability of the electrodes could be verified for 24 hours. Furthermore, our *in-situ* Raman spectroscopic studies have pinpointed the oxidation of Ni preceding the OER process; a direct relation between the activity and the detected Raman signal could be observed. Our results appear to pave the way for establishing Raman spectroscopy as a promising method of choice for identifying the active phase in Ni-bearing systems.

Keywords: Nickel mesh; OER; Raman; iron.

[*]Corresponding authors: i.efthimiopoulos@mpie.de, m.rabe@mpie.de

[†]These authors have contributed equally to this work

I. INTRODUCTION

Ni-based electrodes are a group of promising oxygen evolution reaction (OER) catalysts in alkaline media, owing both to the high catalytic activity and lower productions costs[1–5]. Although the research on Ni-bearing electrodes spans five decades, the exact OER mechanism remains debatable in the literature. The generally accepted picture is that upon immersion of the Ni electrode in an alkaline medium, a layer of a disordered α-$Ni^{2+}(OH)_2$ is spontaneously forming on its surface. Aging of the electrode in an alkaline solution will result in the gradual phase change of α-$Ni(OH)_2$ to the more ordered β-$Ni^{2+}(OH)_2$ variant[6]. Increasing the potential will result in the oxidation of the α-$Ni(OH)_2$ surface species towards the (also disordered) γ-$Ni^{3+}OOH$ phase; oxidation of the β-$Ni^{2+}(OH)_2$ leads to the appearance of the more ordered β-$Ni^{3+}OOH$ modification.

Even though it is not yet clear which oxidized NiOOH phase is the more beneficial for the OER activity, it has been established that the presence of iron promotes the OER performance of the Ni-bearing electrodes in a plethora of Ni-bearing electrode systems[7–11]. Recently, a very simple method for preparing Fe-coated electrodes was reported, which involves the immersion of the Ni-bearing electrode in an Fe-bearing solution[4].

In-situ spectroelectrochemistry has proven to be an efficient tool for understanding the reaction mechanisms during *operando* conditions[3,12,13]. In the majority of Ni-bearing samples, however, such measurements are possible on samples grown on suitable substrates (usually not nickel), which in turn may perplex the interpretation of the obtained results. Hence, the aforementioned preparation method becomes quite appealing for preparing suitable Ni-bearing electrodes directly on nickel substrates, owing to its simplicity and effectiveness.

In this work, we have investigated the OER performance of selected Fe-coated Ni meshes (NM) prepared by directly immersing the respective Ni mesh in Fe-bearing solutions. Indeed, we were able to detect an enhancement of the OER performance for all of our samples. Our *in-situ* Raman spectroscopic studies have captured the potential-induced oxidation of Ni preceding the OER process. Careful analysis of the obtained Raman data has uncovered a direct link between the activity of the NM electrode and the Raman response of the active phase. Such observation may allow Raman spectroscopy to serve as a direct probe and marker of the active phase in Ni-bearing systems.

II. EXPERIMENTAL DETAILS

The nickel mesh (NM) electrodes were provided by De Nora Deutschland GmbH®. The NM samples were cut into 2 × 1 cm^2 and 1 × 1 cm^2 pieces. All of the electrodes were cleaned by 10 min sonication in a 2 M HCl solution (25%, VWR International S.A.S.), rinsed by water and ethanol, and dried by nitrogen gas. Several NM samples were coated by immersion in selected 20 mM Fe-bearing solutions for 30 min (**Table 1**). All solutions in this work are prepared with ultrapure water (18.2 MΩ·cm) at room temperature.

Table 1: Overview of the investigated NM samples. The concentration for each Fe-bearing solution is 20 mM, and the immersion time is 30 min. All samples were cleaned prior to immersion.

Chemical	Company	pH	Sample Name
N/A	N/A	N/A	NM1[a]
$Fe(NO_3)_3 \cdot 9\,H_2O$	Sigma-Aldrich	2.3	NM2
$FeCl_2 \cdot 4\,H_2O$	Carl Roth GmbH	4.2	NM3
$FeCl_3 \cdot 6\,H_2O$	Carl Roth GmbH	2.3	NM4

[a]Ni mesh after cleaning, without any additional treatment.

The NM samples were characterized with normal and grazing incidence X-ray diffraction (XRD, $\lambda_{CuK\alpha}$ = 1.54059 Å), scanning electron microscopy (SEM), Raman, and X-ray photoelectron spectroscopy (XPS) before any electrochemical treatment (*ex-situ*).

Ex-situ XPS was carried out in a Physical Electronics PHI Quantera II spectrometer equipped with an Al-Kα source (= 1486.6 eV). High-resolution oxygen (O 1s) and nickel (Ni $2p_{3/2}$) core level spectra were recorded with a pass energy of 26 eV and an energy step size of 0.025 eV. The acquisition of the survey scan spectra involved a pass energy of 140 eV and an energy step size of 0.1 eV. All measurements were conducted with a take-off angle of 45° and a neutralizer. The C 1s XPS peak of adventitious carbon set at 284.8 eV was used for energy calibration. The processing of the measured spectra was performed with the CasaXPS software[14]. The high-resolution O 1s and Ni $2p_{3/2}$ peaks were fitted with Gaussian (70%) - Lorentzian (30%) peak shape functions (GL30), whereas the first Ni $2p_{3/2}$ component of metallic nickel (~852.6 eV) was fitted with an asymmetric Lorentzian lineshape [LA(1.1, 2.2, 10)] following the suggestion of Biesinger *et al.*[15,16]. A Shirley-type background was applied to all fittings.

The OER activity of nickel meshes was measured with a standard three-electrode system in glass beakers using a Potentiostat (CompacStat P, Ivium). Purified 0.1 M

KOH[17] served as the electrolyte of choice. The working electrode (WE) comprised of one NM sample in contact with a tantalum holder. We should point out that the geometrical working area is kept at 1×1 cm^2 during beaker and *in-situ* experiments for the sake of consistency. An Ag/AgCl electrode (3.4 M KCl, LF-2-100, Innovative Instruments) and a platinum grid acted as the reference (RE) and counter electrode (CE), respectively. All potentials are converted to the reversible hydrogen electrode (RHE) scale using **Eq. 1**:

$$E_{RHE} = E_{Ag/AgCl} + 0.0592 \times pH + 0.199\ V \quad (1)$$

The cyclic voltammetry (CV) curves for each WE consisted of one quick cycle at 50 mV/s for pre-activation, followed by two consecutive 5 mV/s cycles. The electrochemical active surface area (ECSA) was determined using the double-layer capacitance method within a 0.97-0.98 V potential range. Electrochemical impedance spectroscopy (EIS) was carried out using an Autolab potentiostat (AUT50529, Metrohm) at the open circuit potential (OCP) within a 0.1-10^5 Hz frequency range. Tafel slopes were calculated from linear scan voltammetry (LSV) measurements with a potential step of 1 mV and a scan rate of 1 mV/s. Following LSV, each NM sample was subjected to 24 h chronopotentiometric measurements at a current density of 10 mA/cm^2 in order to assess their stability.

Raman spectra were collected with a Labram confocal Raman microscope system (Horiba Jobin Yvon, France), using a ×50 objective lens, a 600 l/mm grating, and a charge-coupled device (CCD) detector. Measurements were performed with a λ = 633 nm Helium-Neon laser. The incident power was ca. 4 mW focused on a 10 μm^2 sample area, with either 3 × 60 s (*ex-situ*) or 90 s (*in-situ*) accumulation time and a spectral resolution of ~1 cm^{-1}. The *in-situ* Raman experiments were conducted with an electrochemical flow-cell (Redox) equipped with a quartz glass window. The WE, RE, and CE were a 1×1 cm^2 NM sample in contact with a Ta holder, an Ag/AgCl electrode (3.4 M KCl, LF-2-100, Innovative Instruments), and a Pt wire, respectively. Raman spectra were collected with three different methodologies during the same experimental run: (a) "dynamic" CV scan (0.94 — 2.23 V, 1 mV/s) with each Raman spectrum representing a 90 mV potential range, (b) "static" scan, with Raman spectra collected at constant potentials (OCP—2.23 V, five accumulations per potential after 5 min equilibration time), and (c) time-dependent Raman measurements at a constant high potential (here @2.23 V).

III. RESULTS AND DISCUSSION

A. *Ex-situ* characterization of the NM electrodes and OER performance

The XRD and grazing incidence XRD patterns [**Fig. 1(a, b)**] do not reveal any visible differences between the pristine and Fe-bearing samples, with all NM XRD patterns indexed with the Ni metal phase. No secondary phases could be detected. Furthermore, the SEM images between the pristine NM1 and the Fe-coated NM2 and NM3 electrodes do not show any particular morphological differences; on the contrary, the NM4 surface appears to be more 'etched' compared to the other samples (**Fig. 2**).

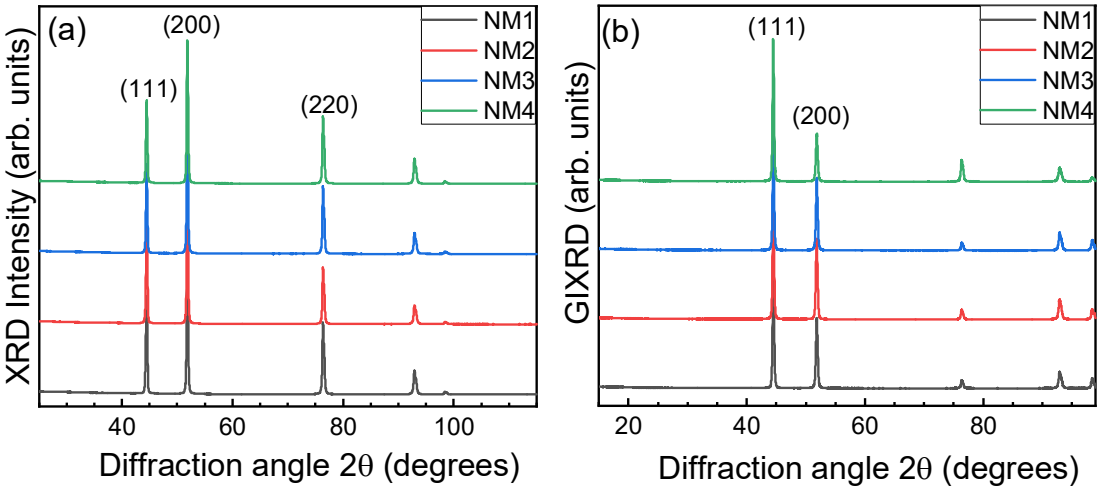

Fig. 1: (a) XRD and (b) grazing incidence XRD patterns for the various NM samples. The patterns can be indexed with the Ni metal phase alone.

More information on the superficial elemental speciation is derived from the XPS measurements (**Fig. 3**). The survey XPS spectra reveal the presence of Ni and O for the NM1 sample, and Ni, O, and Fe for the Fe-coated NM2-NM4 electrodes [**Fig. 3(a)**]. The estimated Ni/Fe ratio is ca. 5.5 for all of the Fe-coated samples, as estimated from the relative areas of the Ni 3p and Fe 3p XPS peaks [inset in **Fig. 3(a)**]. A more elaborate analysis of the high-resolution O1s XPS spectra reveals that the respective envelope can be fitted with either three (NM1 & NM2) or four (NM3 & NM4) components [**Fig. 3(b-e)**].

The O1s XPS region for the NM1 sample can be reproduced with three peaks located at 529.3 eV, 530.9 eV, and 532.3 eV [**Fig. 3(b)**]. These XPS peaks can be attributed to NiO_x, $Ni(OH)_2$, and adsorbed water/ C-O species, respectively[15,16]. A similar deconvolution is performed for the NM2 sample [**Fig. 3(c)**]. On the other hand, the NM3 and NM4 O1s XPS spectra could be fitted with four components, i.e. the three aforementioned contributions with an additional peak at ~529.7 eV. This extra XPS feature can be assigned to the formation of an Fe-O lattice bond[16]. Why would such a

peak not be detected in the Fe-coated NM2 sample as well remains an open issue at this stage. Nevertheless, the O1s analysis reported above allows us to estimate the relative abundance of the NiO_x / $Ni(OH)_2$ species for each NM sample (**Table 2**). We can readily observe that the $Ni(OH)_2$ component is more dominant for the pristine NM1 and the Fe-coated NM4 samples, which exhibit a similar NiO_x / $Ni(OH)_2$ ratio; the situation is more balanced for the NM2 and NM3 samples, where an equal population of NiO_x and $Ni(OH)_2$ is found.

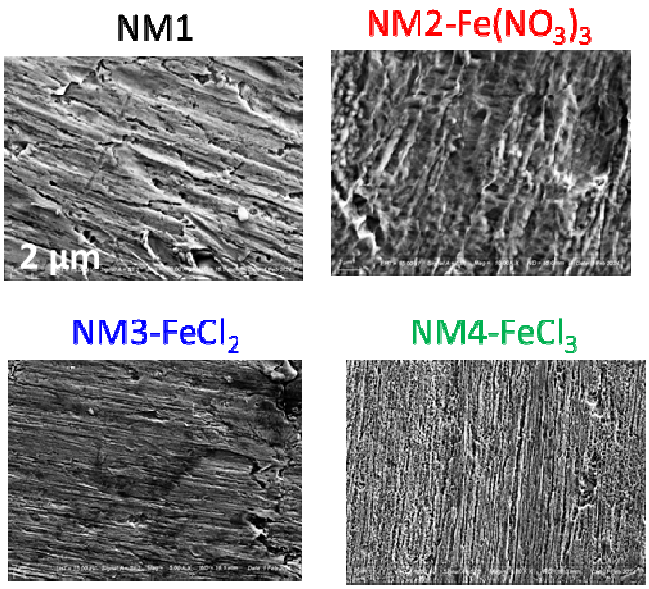

Fig. 2: SEM images of the various NM samples. The scale is 2 µm.

Table 2: The calculated Ni/Fe and NiO_x / $Ni(OH)_2$ ratios for the investigated NM samples, as determined from the XPS survey (Ni 3p & Fe 3p) and the O1s spectra (**Fig. 3**).

Sample	Ni/Fe	NiO_x / $Ni(OH)_2$
NM1	-	0.67
NM2	5.48	1
NM3	5.52	1.03
NM4	5.52	0.66

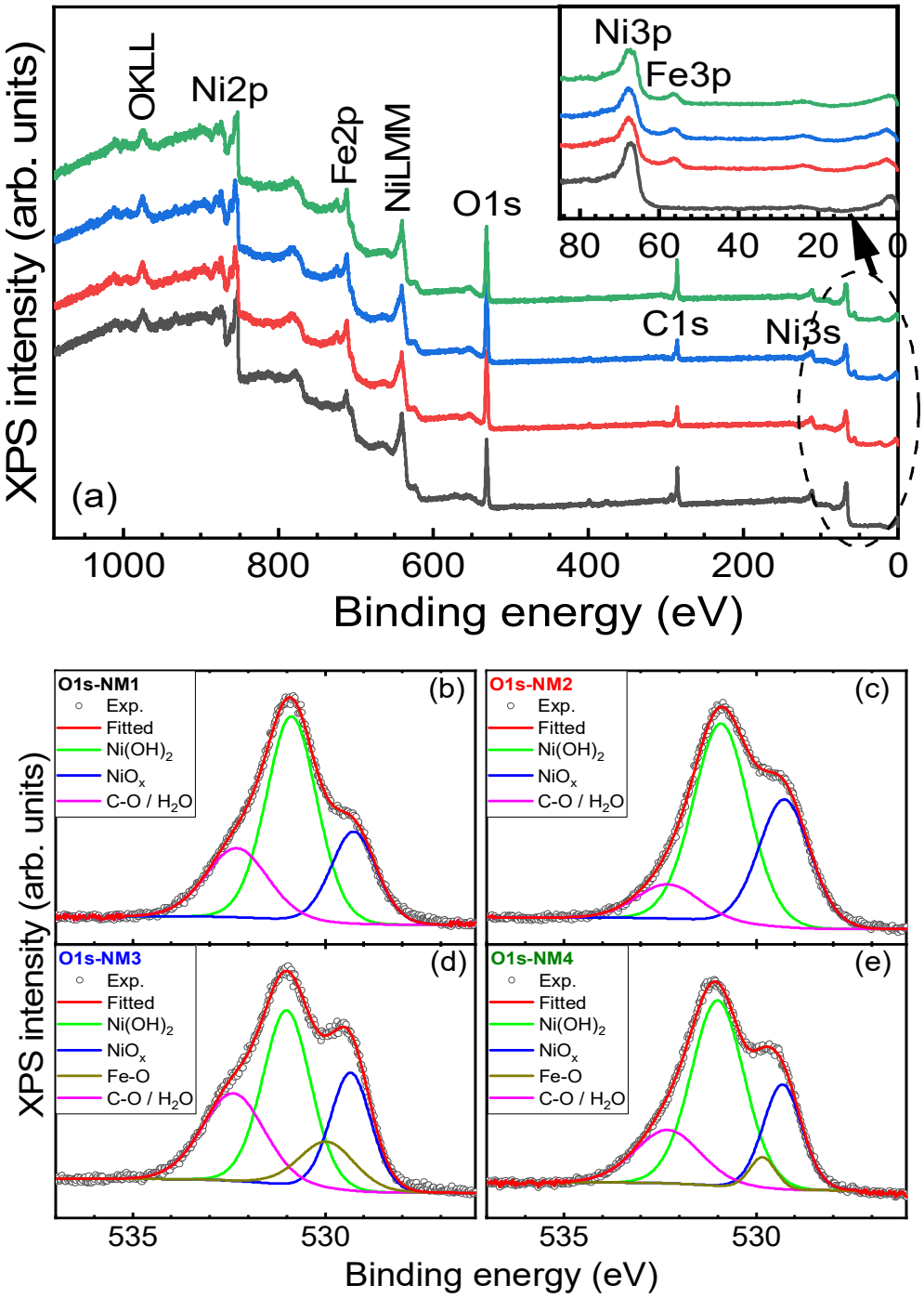

Fig. 3: (a) XPS survey scan spectra of all the measured NM electrodes prior to any treatment. An enhanced view of the adjacent Ni 3p and Fe 3p XPS peaks is also provided in the inset. The high-resolution O1s XPS spectra of the (b) NM1, (c) NM2, (d) NM3, and € NM4 samples are also presented. The respective experimentally measured spectra (open circles) are fitted with $Ni(OH)_2$ (green lines), NiO_x (blue lines), C-O / H_2O (magenta lines), and Fe-O (yellow lines, NM3 & NM4) components. The overall fitting result is depicted as solid red lines passing through the experimental (Exp.) XPS data.

Turning now to the OER Performance of the NM electrodes, **Fig. 4** summarizes the obtained electrochemical results. It is clear that after immersion, the onset potentials (at 0.1 mA/cm^2) of the coated meshes decrease by approximately 0.1 mV from 1.6 V vs. RHE, as shown in the CV scans [**Fig. 4(a)**]. Among all the Fe-coated NM samples, NM2 shows the most significant enhancement in activity, associated with the highest oxidation potential from Ni^{2+} to Ni^{3+} at ca. 1.45 V vs RHE [**Fig. 4(b)**], followed by NM3 as the second most active electrode. The NM4 sample, which is slightly less active compared to NM2 & NM3, shows a lower $Ni^{2+} \rightarrow Ni^{3+}$ oxidation potential (@1.4 V vs RHE) compared to the other samples. The potential increase / decrease of the Ni^{2+} oxidation peak is most likely connected with the phase change from the starting NiO_x / $Ni(OH)_2$ phases present on the Ni surface towards to the β- / γ-NiOOH polymorphs, with the former (latter) being harder (easier) to be oxidized[1,2,18].

The respective Tafel slopes were obtained by LSV with a scan rate of 1 mV/s [**Fig. 4(c)**]. There is an obvious change in the Tafel slope after immersion. The pristine NM1 sample has a slope of 61.8 mV/dec, while the Fe-coated NM range from 45 mV/dec to 50 mV/dec, close to the reported value of 46 mV/dec for Ni β /β [5,19,20]. In order to assess the stability of the NM samples, an aging chronopotentiometric experiment at 10 mA/cm^2 was carried out for 24 hours. In Fig. **4(d)** we can observe that the Fe-coated samples show a minor degradation within this timeframe; the pristine NM1, however, shows a relatively sharp increase in its potential during the first 5 hours, followed by a more moderate degradation after that time, indicating that the NM1 active phase is deteriorating more rapidly without the presence of iron.

The aforementioned electrochemical parameters are compiled in **Fig. 4(e)**. We should point out here that the most active NM2 and NM3 samples show the smallest ECSA values; one possible explanation might be that the almost equivalent population of the NiO_x / $Ni(OH)_2$ species on the surface of these samples (**Table 2**), alongside the participation of iron, effectively blocks active surface sites in these NM electrodes. Interestingly, the NM4 sample with a dominant $Ni(OH)_2$ surface phase (**Table 2**), shows a larger ECSA, concomitant with its activity enhancement. Another interesting differentiation between the Fe-coated NM samples involves the I_{pa}/I_{pc} parameter, which represents the intensity ratio of the redox peaks. A ratio value larger than unity, as found for the NM1 and NM4 electrodes, indicates a poor reversibility of the reaction process, which in turn may be caused by the spontaneous decomposition of the Ni^{3+} active phase and/or ion dissolution during the OER process [19–23].

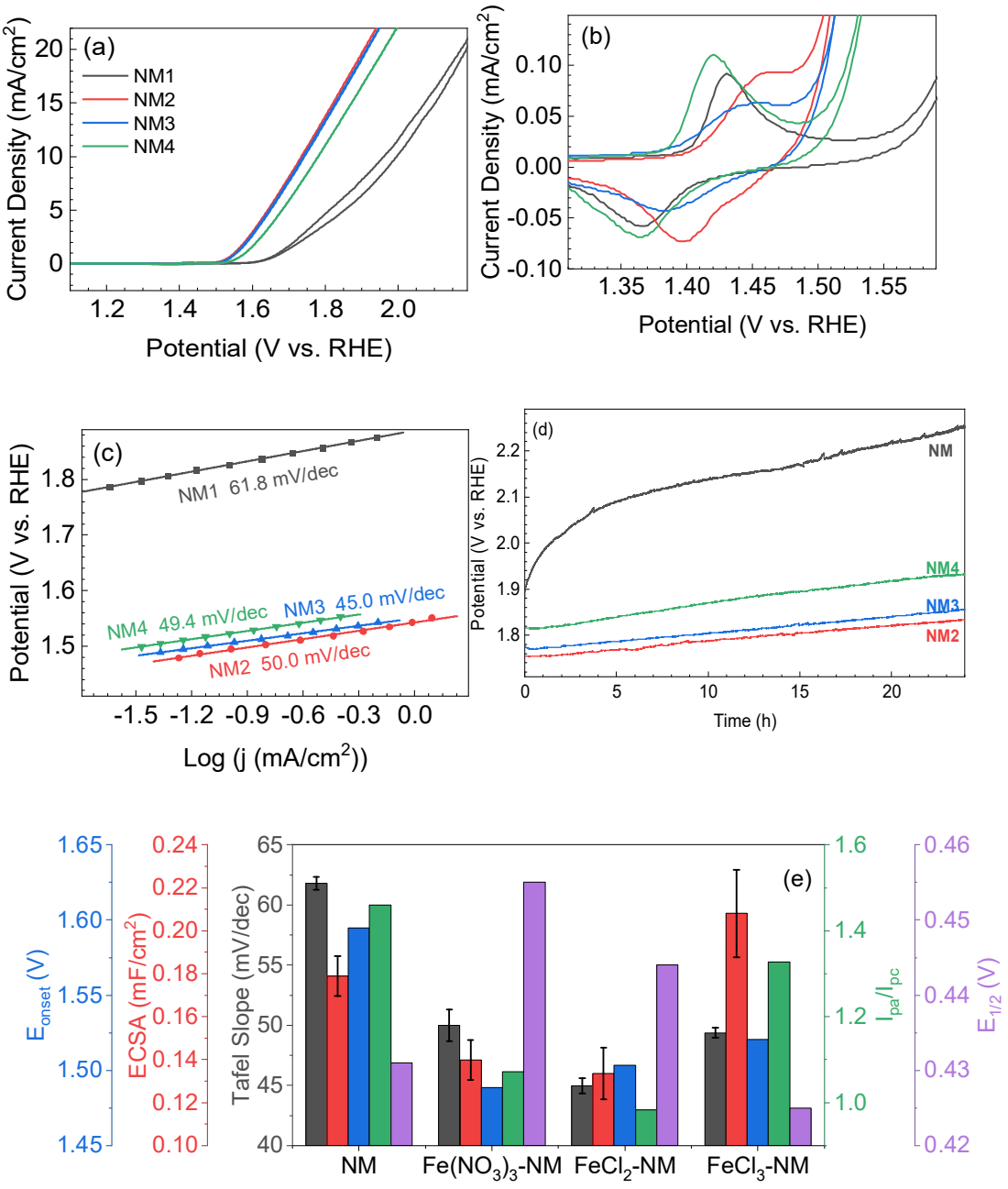

Fig. 4: (a) CV scans for all NM samples (5 mV/s, 0.1 M KOH). (b) Enhanced view of the $Ni^{2+} \rightarrow Ni^{3+}$ oxidation peaks. (c) LSV scans with the respective Tafel slopes for all NM samples. (d) Chronopotentiometric study for all the NM samples performed at 10 mA/cm^2 for 24 hours. (e) Compilation of the obtained electrochemical parameters for all of the investigated NM samples.

The latter scenario was tested with *in-situ* ICP-MS measurements with a scanning flow cell for all NM samples. The results are shown in **Fig. 5.** A small amount of dissolving Ni was detected in the high potential range for the pristine NM1 sample during the first CV cycle. Such Ni dissolution could not be observed for any of the Fe-coated samples. Furthermore, no Fe dissolution was found for any of the NM samples. Hence, we can assume that the high value of the I_{pa}/I_{pc} parameter for the NM4 sample is most likely connected with the spontaneous decomposition of the formed Ni^{3+} active phase during the OER process.

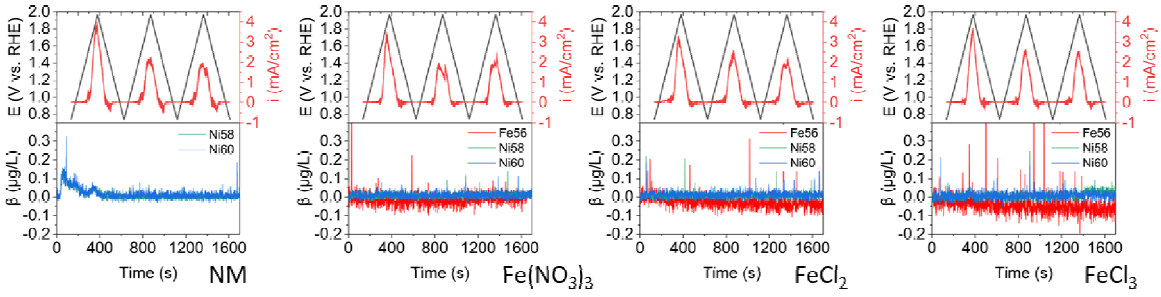

Fig. 5: *In-situ* **s**canning-flow cell ICP-MS measurements for all of the investigated NM samples during Cyclic Voltammetry in Fe-free 0.01 M KOH. The blue and red curves stand for the Ni and Fe ions, respectively.

B. Raman spectroscopic investigations of the NM electrodes before and during the OER process

Additional insights on the structural properties on the NM electrodes is obtained from Raman spectroscopy. Initially we show the *ex-situ* Raman spectra for all of our samples (**Fig. 6**). Comparison of the Raman spectra reveals noticeable differences. In particular, the Raman response of the NM1 and NM3 samples is rather featureless, implying that either the surface is not sufficiently oxidized, i.e. not enough volume of oxidized NiO_x / $Ni(OH)_2$ species, and/or that the phases formed on the electrode surface are heavily disordered. On the other hand, both the NM2 and NM4 samples yield a measurable Raman spectrum, with two Raman peaks appearing at 517 cm^{-1} and 650 cm^{-1} (NM2) and 523 cm^{-1} and 680 cm^{-1} (NM4). The Raman profile is compatible with the presence of NiO_x[6,24–26]. The variation between the Raman peak frequencies of the Fe-coated NM2 and NM4 samples may be rationalized by the more effective incorporation of Fe^{3+} in the NiO_x lattice of NM4, as revealed by the detection of an Fe-related component in the O1s XPS spectra [**Fig. 3(e)**]; such incorporation of the smaller Fe^{3+} would induce a Raman shift towards higher frequencies. Regarding the presence of the $Ni(OH)_2$ species, as inferred from the XPS analysis (**Fig. 3 & Table 2**), we can probably exclude the presence of β-$Ni(OH)_2$ in our NM2 and NM4 Raman spectra, as we do not detect the characteristic Raman peaks at ca. 320 cm^{-1} and 450 cm^{-1}. On the

other hand, the presence of α-Ni(OH)$_2$ cannot be unequivocally excluded, as its Raman signal may strongly overlap with the Raman response of NiO_x [6,24–26].

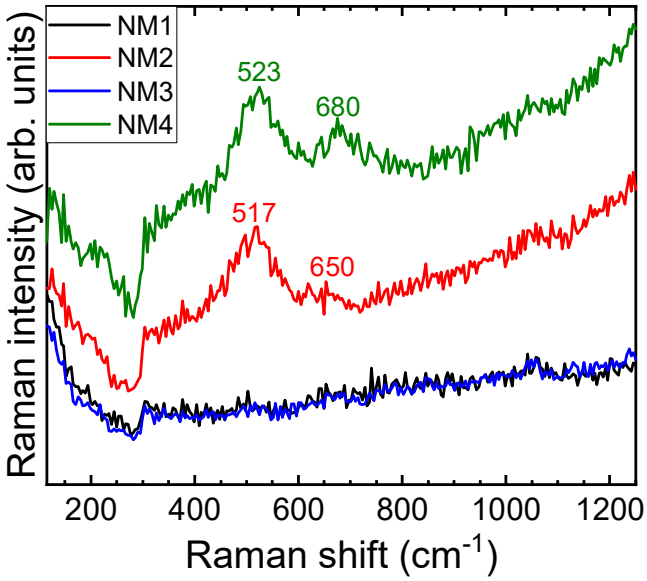

Fig. 6: Raman spectra of the various NM samples collected *ex-situ* (λ = 633 nm).

Turning to our *in-situ* Raman measurements, the results of our 'dynamic' scans are shown in **Fig. 7**. For all samples, we detect the appearance of two new Raman modes at 470-480 cm^{-1} and at 550-560 cm^{-1} close to 1.47 V vs RHE, i.e. at the oxidation potential of $Ni^{2+} \rightarrow Ni^{3+}$ [**Fig. 4(b)**]. These peaks are assigned to the bending and stretching vibrations of the NiO_6 octahedra comprising the oxidized NiOOH phase[13,21,27,28]. We should point out that the recorded CV curves during the 'dynamic' Raman measurements are qualitatively similar to their beaker counterparts (not shown). The 'static' Raman measurements show also the appearance of the NiOOH Raman features close to the oxidation potential for each NM sample.

Even though the acquired Raman response is similar for all NM samples during the OER process, certain differences could be detected for the active NiOOH phase. In **Fig. 8** we present an overview of our 'static' Raman measurements at 2.23 V vs RHE, i.e. Raman spectra collected by keeping the potential constant well above the OER process. By analyzing the Raman-related parameters of the NiOOH phase for all NM samples, we can immediately observe that the more active NM2 and NM3 samples exhibit lower NiOOH Raman shifts compared to the less active NM1 and NM4 electrodes [**Fig. 8(b)**]. This observation seems quite puzzling at a first glance, as a direct correlation between the OER activity and the Raman response of the active phase has not been reported in Ni electrodes.

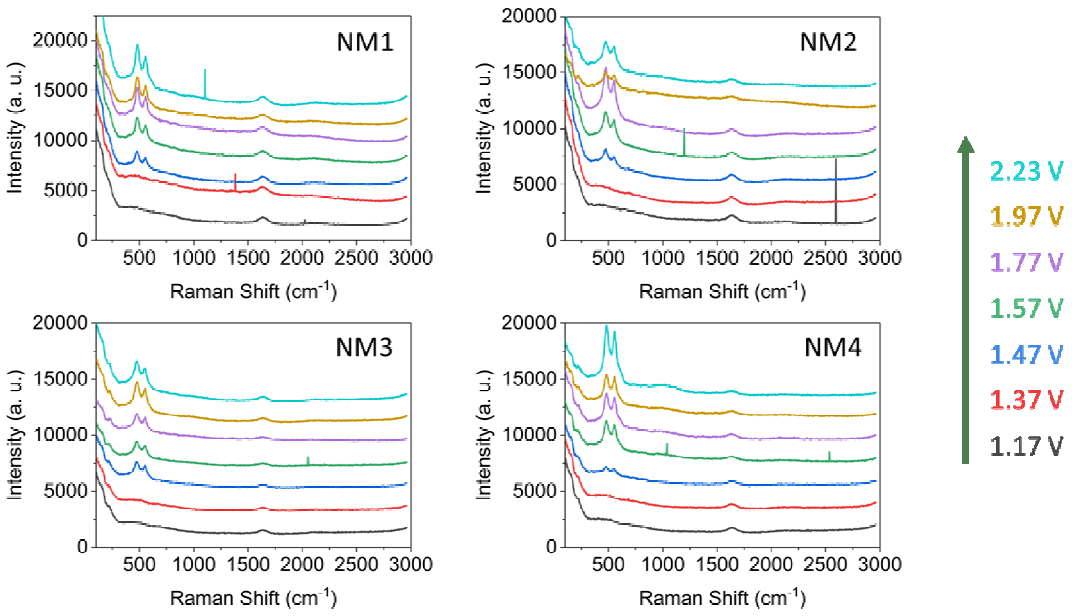

Fig. 7: *In-situ* Raman spectra of the various NM samples collected during a 'dynamic' CV scan ($\lambda = 633$ nm).

A possible explanation might be that we detect two types of NiOOH phases in our NM Raman spectra, namely the β-NiOOH polymorph for the NM2 and NM3 electrodes, and the γ-NiOOH modification for the NM1 and NM4 samples. Evidence to support this scenario is (a) the higher oxidation potentials for the NM2 and NM3 samples recorded typical for β-NiOOH [**Fig. 4(b)**][9–11,29–31], and (b) the average higher Ni valence of the γ-NiOOH phase is expected to result in shorter Ni-O distances compared to β-NiOOH[32], thus in larger shifts for the two Raman-active modes.

We should finally mention that, unlike earlier reports[29,33], we were not able to detect a clear correlation between the Raman intensity ratio of the NiOOH phase and the activity of the electrode.

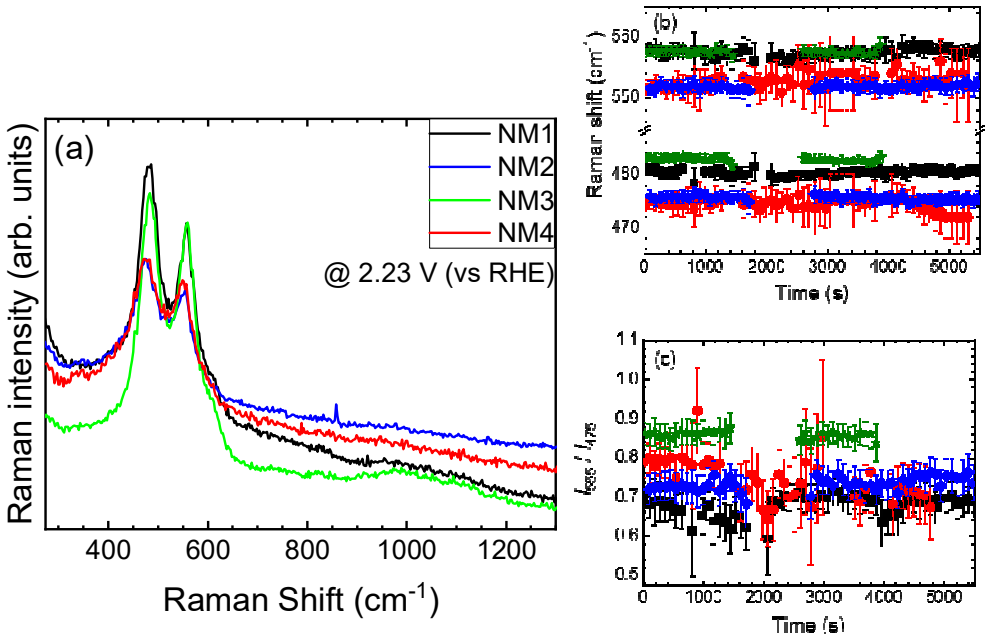

Fig. 8: (a) Representative Raman spectra and time dependence of the (b) Raman shifts and (c) Raman peak intensity ratio of the NiOOH phase for all of the NM samples collected at 2.23 V vs RHE.

CONCLUSIONS

In summary, we have investigated the OER performance of Ni meshes coated with iron. The coating was achieved by direct immersion of the Ni mesh sample on selected Fe-bearing solutions. In all cases, we were able to detect an enhancement of the OER performance, with the NM samples immersed in 20 mM $Fe(NO_3)_3$ and 20 mM $FeCl_2$ solutions showing the best activity. The stability of the electrodes could be verified for 24 hours.

Quite surprisingly, our in-situ Raman spectroscopic studies have additionally uncovered a direct correlation between the activity of the Ni electrodes and the Raman shift of the respective NiOOH active phase. Our current understanding is that a different NiOOH polymorph is forming in each case after the oxidation potential of nickel, which would in turn allow for Raman spectroscopy to be used as a marker for identifying the exact active phase in Ni-bearing systems.

Acknowledgements

This work was funded by the German Federal Ministry of Education and Research (BMBF project "PrometH2eus", FKZ 03HY105J). This work is funded by the Deutsche Forschungsgemeinschaft (DFG, German Research Foundation) under Germany's Excellence Strategy - EXC 2033 - 390677874 – RESOLV.

REFERENCES

[1] A. Audemer, A. Delahaye, R. Farhi, N. Sac-Epée, and J. -M. Tarascon, J. Electrochem. Soc. **144**, 2614 (1997).

[2] M.C. Bernard, M. Keddam, H. Takenouti, P. Bernard, and S. Sényarich, J. Electrochem. Soc. **143**, 2447 (1996).

[3] Y. Zhai, Z. Zhu, S. Zhou, C. Zhu, and S. Dong, Nanoscale **10**, 3089 (2018).

[4] H. Yin, L. Jiang, P. Liu, M. Al-Mamun, Y. Wang, Y.L. Zhong, H. Yang, D. Wang, Z. Tang, and H. Zhao, Nano Res. **11**, 3959 (2018).

[5] Z. Qiu, Y. Ma, and T. Edvinsson, Nano Energy **66**, 104118 (2019).

[6] D.S. Hall, D.J. Lockwood, C. Bock, and B.R. MacDougall, Proc. R. Soc. A **471**, 20140792 (2015).

[7] D.A. Corrigan and S.L. Knight, J. Electrochem. Soc. **136**, 613 (1989).

[8] L. Ciambriello, E. Cavaliere, I. Vassalini, I. Alessandri, M. Ferroni, L. Leoncino, R. Brescia, and L. Gavioli, J. Phys. Chem. C **126**, 21759 (2022).

[9] D. Friebel, M.W. Louie, M. Bajdich, K.E. Sanwald, Y. Cai, A.M. Wise, M.-J. Cheng, D. Sokaras, T.-C. Weng, R. Alonso-Mori, R.C. Davis, J.R. Bargar, J.K. Nørskov, A. Nilsson, and A.T. Bell, J. Am. Chem. Soc. **137**, 1305 (2015).

[10] M. G\''orlin, P. Chernev, J.F. de Araújo, T. Reier, S. Dresp, B. Paul, R. Krähnert, H. Dau, and P. Strasser, J. Am. Chem. Soc. **138**, 5603 (2016).

[11] M. G\''ojrlin, J.F. de Araújo, H. Schmies, D. Bernsmeier, S. Dresp, M. Gliech, Z. Jusys, P. Chernev, R. Kraehnert, H. Dau, and P. Strasser, J. Am. Chem. Soc. **139**, 2070 (2017).

[12] M. Rabe, C. Toparli, Y.-H. Chen, O. Kasian, K.J.J. Mayrhofer, and A. Erbe, Phys. Chem. Chem. Phys. **21**, 10457 (2019).

[13] D.S. Hall, D.J. Lockwood, S. Poirier, C. Bock, and B.R. MacDougall, ACS Appl. Mater. Interfaces **6**, 3141 (2014).

[14] N. Fairley, V. Fernandez, M. Richard-Plouet, C. Guillot-Deudon, J. Walton, E. Smith, D. Flahaut, M. Greiner, M. Biesinger, S. Tougaard, D. Morgan, and J. Baltrusaitis, Appl. Surf. Sci. Adv. **5**, 100112 (2021).

[15] M.C. Biesinger, B.P. Payne, L.W.M. Lau, A. Gerson, and R.S.C. Smart, Surf. Interface Anal. **41**, 324 (2009).

[16] M.C. Biesinger, B.P. Payne, A.P. Grosvenor, L.W.M. Lau, A.R. Gerson, and R.S.C. Smart, Appl. Surf. Sci. **257**, 2717 (2011).

[17] I. Spanos, M.F. Tesch, M. Yu, H. Tüysüz, J. Zhang, X. Feng, K. Müllen, R. Schlögl, and A.K. Mechler, ACS Catal. **9**, 8165 (2019).

[18] B. Beden, D. Floner, J.M. Léger, and C. Lamy, Surf. Sci. **162**, 822 (1985).

[19] Z. Qiu, C.W. Tai, G.A. Niklasson, and T. Edvinsson, Energy Environ. Sci. **12**, 572 (2019).

[20] P. Oliva, J. Leonardi, J.F. Laurent, C. Delmas, J.J. Braconnier, M. Figlarz, F. Fievet, and A. d. Guibert, J. Power Sources **8**, 229 (1982).

[21] H. Radinger, P. Connor, S. Tengeler, R.W. Stark, W. Jaegermann, and B. Kaiser, Chem. Mater. **33**, 8259 (2021).

[22] N.A. Saguì, P. Ström, T. Edvinsson, and İ. Bayrak Pehlivan, ACS Catal. **12**, 6506 (2022).

[23] S.S. Jeon, P.W. Kang, M. Klingenhof, H. Lee, F. Dionigi, and P. Strasser, ACS Catal. **13**, 1186 (2023).

[24] A.Y. Faid, A.O. Barnett, F. Seland, and S. Sunde, Electrochim. Acta **361**, 137040 (2020).

[25] C. Johnston and P.R. Graves, Appl. Spectrosc. **44**, 105 (1990).

[26] N. Mironova-Ulmane, A. Kuzmin, I. Steins, J. Grabis, I. Sildos, and M. Pärs, J. Phys. Conf. Ser. **93**, 12039 (2007).

[27] C.A. Melendres and S. Xu, J. Electrochem. Soc. **131**, 2239 (1984).

[28] R.A. Marquez, E. Kalokowski, M. Espinosa, J.T. Bender, Y.J. Son, K. Kawashima, C.E. Chukwuneke, L.A. Smith, H. Celio, A. Dolocan, X. Zhan, N. Miller, D.J. Milliron, J. Resasco, and C.B. Mullins, Energy & Environ. Sci. (2024).

[29] B.S. Yeo and A.T. Bell, J. Phys. Chem. C **116**, 8394 (2012).

[30] S. Lee, L. Bai, and X. Hu, Angew. Chemie Int. Ed. **59**, 8072 (2020).

[31] S. Klaus, Y. Cai, M.W. Louie, L. Trotochaud, and A.T. Bell, J. Phys. Chem. C **119**, 7243 (2015).

[32] M. MORISHITA, S. OCHIAI, T. KAKEYA, T. OZAKI, Y. KAWABE, M. WATADA, S. TANASE, and T. SAKAI, Electrochemistry **76**, 802 (2008).

[33] M.W. Louie and A.T. Bell, J. Amer. Chem. Soc. **135**, 12329 (2013).